Research Article | Open Access

Microstructures

Xu *et al*. *Microstructures* **2026**, *6*, 20260135 **DOI:**10.20517/microstructures.2026.39

Control of magnetic anisotropy in epitaxial $SrRuO_3$ via oxygen octahedral engineering

Zedong Xu[1,2], Linxue Chai[1], Sixia Hu[2], Mao Ye[3], Shanquan Chen[2], Yong Jiang[1], Lang Chen[2]

Keywords:
Transition metal oxides, $SrRuO_3$, crystal symmetry control, magnetic anisotropy, oxygen octahedral engineering

Citation: Xu, Z.; Chai, L.; Hu, S.; Ye, M.; Chen, S.; Jiang, Y.; Chen, L. Control of magnetic anisotropy in epitaxial $SrRuO_3$ via oxygen octahedral engineering. *Microstructures* **2026**, *6*, 20260135. https://dx.doi.org/10.20517/microstructures.2026.39

Received: 21 Mar 2026
First Decision: 26 May 2026
Revised: 3 Sep 2026
Accepted: 4 Sep 2026
Published: 26 Oct 2026

Academic Editor:
Jun Chen
Copy Editor:
Ping Zhang
Production Editor:
Ping Zhang

Check for updates

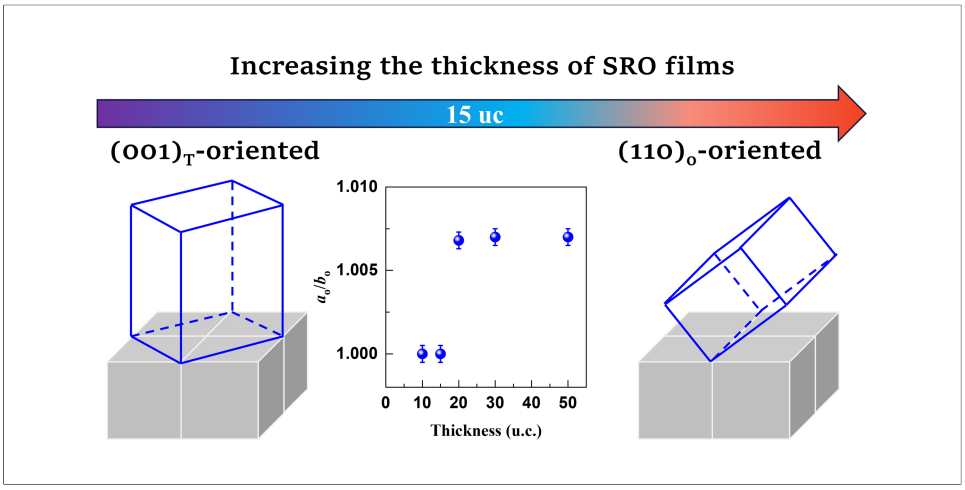

Abstract

In transition metal oxides, strong electron, spin, and lattice correlations originating from *d-p* orbital hybridization govern their functional properties. These functional properties are highly sensitive to their lattice symmetry. Here we demonstrate the control of crystal symmetry in $SrRuO_3$ by engineering a $SrTiO_3/SrRuO_3$ heterointerface with atomic-scale thickness variation. Proximity to the cubic $SrTiO_3$ substrate can induce a non-tilted RuO_6 configuration, stabilizing a tetragonal phase in ultrathin $SrRuO_3$. As the thickness of $SrRuO_3$ film increases, the structure transitions toward a monoclinic-distorted orthorhombic symmetry. High-resolution X-ray diffraction confirms this evolution. The films within the critical thickness range exhibit tetragonal symmetry, enhanced saturation magnetization, and isotropic in-plane magnetism, whereas thicker films become a monoclinic-distorted

[1]Institute of Quantum Materials and Devices, and Tianjin Key Laboratory of Optoelectronic Detection Technology and System, School of Electronics and Information Engineering; State Key Laboratory of Separation Membranes and Membrane Processes, School of Materials Science and Engineering, Tiangong University, Tianjin 300387, China.
[2]Department of Physics, and State Key Laboratory of Quantum Functional Materials, and Guangdong Basic Research Center of Excellence for Quantum Science, Southern University of Science and Technology, Shenzhen 518055, Guangdong, China.
[3]School of Physics and Materials Science, Guangzhou University, Guangzhou 510006, Guangdong, China.

Correspondence to: Prof. Zedong Xu, Institute of Quantum Materials and Devices, and Tianjin Key Laboratory of Optoelectronic Detection Technology and System, School of Electronics and Information Engineering; State Key Laboratory of Separation Membranes and Membrane Processes, School of Materials Science and Engineering, Tiangong University, Tianjin 300387, China; Department of Physics, and State Key Laboratory of Quantum Functional Materials, and Guangdong Basic Research Center of Excellence for Quantum Science, Southern University of Science and Technology, Shenzhen 518055, Guangdong, China. E-mail: xuzedong@tiangong.edu.cn; Prof. Yong Jiang, Institute of Quantum Materials and Devices, and Tianjin Key Laboratory of Optoelectronic Detection Technology and System, School of Electronics and Information Engineering; State Key Laboratory of Separation Membranes and Membrane Processes, School of Materials Science and Engineering, Tiangong University, Tianjin 300387, China. E-mail: yjiang@tiangong.edu.cn; Prof. Lang Chen, Department of Physics, and State Key Laboratory of Quantum Functional Materials, and Guangdong Basic Research Center of Excellence

for Quantum Science, Southern University of Science and Technology, Shenzhen 518055, Guangdong, China. E-mail: chenlang@sustech.edu.cn

orthorhombic phase with strong in-plane magnetic anisotropy. This work establishes oxygen octahedral engineering as a powerful method for tailoring magnetic anisotropies in transition metal oxides.

INTRODUCTION

Quantum materials are a class of matter whose macroscopic properties are governed by quantum mechanical effects[1,2]. Owing to their unique quantum behaviors, these systems have attracted extensive research interest for their promising applications in quantum technologies and spintronics[3]. Among them, a family of 4*d* ruthenium oxides has garnered particular attention. These materials are typically excellent conductors featuring ruthenium in the Ru^{4+} oxidation state. For instance, RuO_2 has recently been identified as a prototypical altermagnet[4,5]. Its crystal structure features opposite-spin sublattices connected via rotational symmetry, a unique spin group, zero net magnetization, and a characteristic *d*-wave pattern of time-reversal symmetry-breaking spin splitting on its Fermi surfaces. Sr_2RuO_4, with a superconducting critical temperature of 1.5 K, most likely exhibits a chiral *p*-wave spin-triplet state with broken time-reversal symmetry, although its precise order parameter remains under debate[6-8]. $SrRuO_3$ (SRO) stands as a ferromagnetic Weyl semimetal that exhibits nonmonotonic temperature dependence of both anomalous Hall conductivity and spin-wave gap[9-11]. For the 4*d* ferromagnetic SRO, the magnetic properties are highly sensitive to its lattice symmetry[12-14]. This symmetry can be tuned via oxygen displacements from their face-center sites, which alter the transition metal-oxygen bond lengths and angles[15,16]. These structural changes manifest as tilts or rotations of the oxygen octahedra. Although epitaxial strain is a common tool for manipulating the octahedral distortions, the structural changes it produces are complex. Recently, the results demonstrate that interface engineering of the oxygen coordination environment allows one to control additional degrees of freedom in SRO films[17,18]. Interface engineering has thus been recognized as a promising route for controlling the octahedral tilts in the heterostructure. The interfacial coupling has a short impact length scale, unlike strain. This allows us to tailor the structural symmetry and magnetic properties by controlling the thickness of SRO films, rather than introducing oxygen vacancies in previous work[13,19]. Introducing defects can affect the magnetic moment for SRO film.

In this Article, we modulate the crystal symmetry of SRO by fabricating a $SrTiO_3$ (STO)/SRO heterointerface with mismatched lattice symmetry and exerting atomic-level control over the SRO layer thickness. Near the STO/SRO interface, the RuO_6 follows the non-tilted STO structure due to the cubic symmetry in STO, thereby suppressing octahedral tilting in ultrathin SRO films and stabilizing a tetragonal phase. As the film thickness increases, the octahedral tilts in thicker films approach the orthorhombic symmetry in SRO. Experimentally, high-resolution X-ray diffraction (XRD) is used to confirm such a structural symmetry transition. The corresponding critical thickness is about 15-unit cells (uc). Below 15 uc of thickness, the SRO films exhibit a tetragonal lattice symmetry, enhanced saturation magnetization, and isotropic in-plane magnetic behavior. In contrast, beyond 15 uc, the SRO lattice symmetry is monoclinic-distorted orthorhombic, similar as bulk SRO, with a strong in-plane magnetic anisotropy. As a result, we demonstrate the control of the lateral magnetic anisotropies by atomic-scale symmetry design of the oxygen coordination environment in SRO films.

MATERIALS AND METHODS

Epitaxial SRO thin films with different thicknesses were prepared on the TiO_2-terminated (001) STO substrates via pulsed laser deposition (PLD). Film growth was performed using a KrF excimer laser (248 nm wavelength) with a laser fluence of 2 J cm^{-2} and a repetition rate of 13 Hz, under an oxygen atmosphere of

100 mTorr and a substrate temperature of 680 °C. A commercial 99.99%-purity SRO ceramic target (Kurt J. Lesker Company) was adopted for deposition, with the target-substrate distance fixed at 4.5 cm. The film thickness was monitored *in situ* by reflection high-energy electron diffraction (RHEED) throughout the growth process [Supplementary Figure 1]. To explore the thickness-dependent structural phase evolution and magnetic anisotropy of SRO films, samples with thicknesses of 10, 15, 20, 30, and 50 uc were prepared and systematically investigated.

The crystal structure of the epitaxial SRO films was characterized by XRD, including a 2θ-ω scan of the (002) reflection and reciprocal space mapping of the STO substrate (204) peak at φ = 0°, 90°, 180°, and 270°. Surface topography was investigated by atomic force microscopy (AFM) over a scanning area of 5 × 5 μm^2. Magnetic hysteresis (*M-H*) loops were acquired at 10 K using a Quantum Design superconducting quantum interference device (SQUID) magnetometer (MPMS) along the (100), (010), and (001) crystallographic orientations of the STO substrate. Hall transport properties were evaluated with a physical property measurement system (PPMS).

RESULTS AND DISCUSSION

Figure 1A displays the schematic diagram of SRO thin films grown on STO substrates. Figure 1B presents the XRD 2θ-ω scan spectrum of the as-prepared SRO films. Clear Laue fringes around the SRO (002) diffraction peak are observed for our epitaxial SRO films on STO substrates. We further performed XRD rocking curve measurements on all SRO thin films, as presented in Supplementary Figure 2. Narrow full width at half-maximum (FWHM) values of 0.105°, 0.098°, 0.093°, 0.082°, and 0.076° were obtained for the SRO (002) diffraction peaks corresponding to film thicknesses of 10, 15, 20, 30, and 50 uc, respectively. The presence of pronounced Laue oscillations and sharp rocking curves demonstrates the high crystalline uniformity of the SRO films on STO substrates. With increasing SRO film thickness, the SRO (002) diffraction peaks gradually shift toward higher Bragg angles, indicating a lattice shortening along the out-of-plane *c*-axis. The pseudo-cubic *c*-axis lattice parameters extracted from the SRO (002) peak positions are plotted as a function of film thickness in Figure 1C, which reveals a monotonic decrease in the *c*-lattice constant with increasing film thickness. Additionally, AFM characterization reveals a uniform step-terrace morphology for the 10 uc SRO film, demonstrating an atomically smooth surface [Figure 1D]. SRO films with different thicknesses exhibit analogous step-terrace surface topography, with only minor variations in terrace width stemming from slight differences in the cutting angle of commercial STO substrates [Supplementary Figure 3]. These morphological features further verify the excellent epitaxial quality of the SRO films.

The crystal structure of the SRO film was further examined by reciprocal space mappings (RSMs) using high-resolution XRD (HRXRD). RSMs were acquired around the asymmetric STO (204) Bragg reflection at φ = 0°, 90°, 180°, and 270° to evaluate the epitaxial strain and structural coherence of SRO films. We observe that the structural symmetry of SRO films changes from tetragonal to monoclinic-distorted orthorhombic with increasing the thickness of SRO films. Figure 2A presents the RSM results for 15 uc SRO films. Note that the *z* direction corresponds to the out-of-plane direction of the sample surface plane. Both the film and substrate peaks exhibit the same Q_X values across the RSM patterns, demonstrating that all films are coherently strained to match that of the STO substrate and possess identical in-plane lattice parameters. For the 15 uc SRO film, the diffraction peaks occur at the same Q_Z value across different azimuthal φ angles, which is characteristic of a tetragonal structure[20,21]. The corresponding structural schematic of the tetragonal phase is illustrated in Figure 2B[13]. The out-of-plane orientation is along the $(001)_T$ of SRO with a notably elongated lattice constant c_T. In this configuration, the Ru-O-Ru bond angle θ, which determines the octahedral tilting degree calculated as $(180°-\theta)/2$, aligns along the out-of-plane direction. In contrast, the 30 uc SRO film shows distinct Q_Z variations at different azimuthal φ angles, verifying a monoclinic-distorted

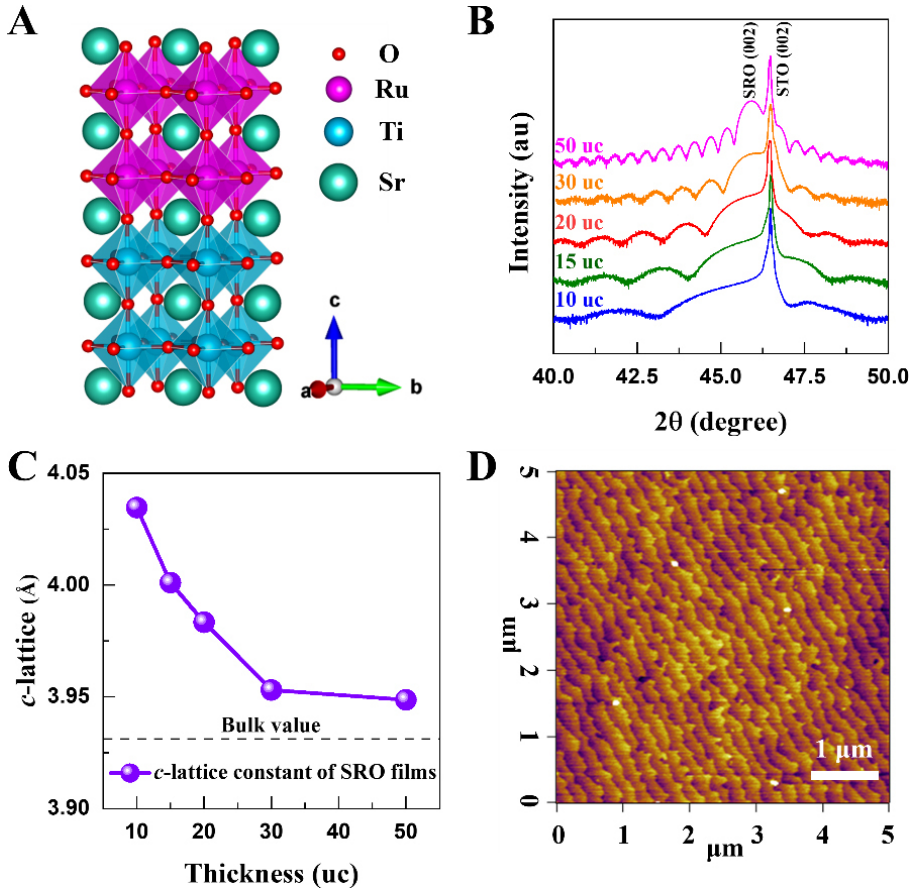

Figure 1. Structural characterization of SRO films grown on STO (001) substrates at room temperature. (A) Schematics of the SRO and STO crystal structure; (B) 2θ-ω XRD scans of the epitaxial SRO films around the STO (002) peak with variable thickness; (C) Lattice constant *c* *vs.* thickness of SRO film. The black dotted line represents the pseudo-cubic *c*-lattice of bulk SRO; (D) The AFM topography images of the SRO film, offering a visual representation of its surface. SRO: $SrRuO_3$; STO: $SrTiO_3$; XRD: X-ray diffraction; AFM: atomic force microscopy; uc: unit cells.

orthorhombic structure [Figure 2C], and the corresponding structural schematic is presented in Figure 2D. Here, the out-of-plane direction corresponds to the $(110)_o$ plane of SRO, while the c_o axis lies in the film plane and is fully constrained by the substrate. In this case, the Ru-O-Ru bond angle θ tilts along the in-plane direction. We determined the room-temperature lattice parameters of the 30 uc SRO film as a_o = 5.58 Å, b_o = 5.54 Å, c_o = 7.81 Å, $\alpha_o = \beta_o$ = 90°, and γ_o = 89.3°. To distinguish between orthorhombic and tetragonal phases, we define an orthorhombicity factor as the ratio a_o/b_o[21]. The orthorhombicity factor is 1.007 for 30 uc SRO film. In contrast, for the 15 uc film, the orthorhombicity factor is 1.000. The thickness-dependent evolution of a_o/b_o is summarized in Figure 3. The plotted trend reveals that lattice symmetry transition takes place at a critical thickness of 15 uc, which is in good agreement with previous studies[21]. SRO films with thicknesses above the critical value adopt a stable monoclinic-distorted orthorhombic phase, while thinner films retain the tetragonal phase.

The octahedral tilt angle of SRO thin films, which correlates structural symmetry with internal lattice distortion, can be quantitatively calculated from the orthorhombicity factor through the following empirical formula:

$$\frac{b_o}{a_o} = \frac{b^{oct}}{a^{oct}} cos\left(\frac{180° - \theta}{2}\right) \quad (1)$$

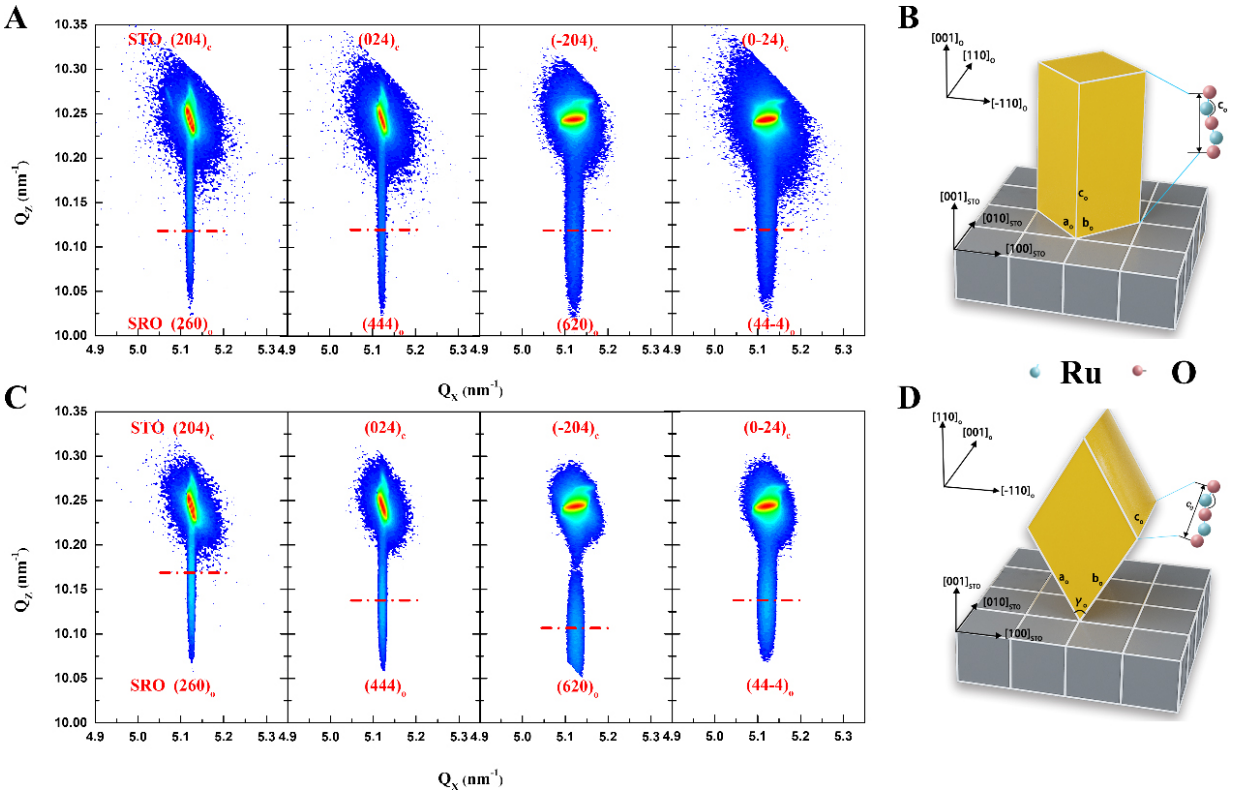

Figure 2. (A) RSMs of 15 uc SRO films grown on STO substrates measured at room temperature; (B) Corresponding schematic diagram illustrating the tetragonal structure of SRO films grown on STO substrates; (C) RSMs of 30 uc SRO films grown on STO substrates measured at room temperature; (D) Schematic diagram showing the orthorhombic structure of SRO films grown on STO substrates. The peak positions of the SRO $(260)_o$, $(444)_o$, $(620)_o$, and $(44\text{-}4)_o$ reflections, corresponding to STO (204), (024), (-204), and (0-24), respectively. Figure 2B and D, adapted from[13], Copyright 2013, AIP Publishing. SRO: $SrRuO_3$; STO: $SrTiO_3$; RSMs: reciprocal space mappings.

Here, the ratio b^{oct}/a^{oct} denotes the bond length in a RuO_6 octahedron. As previously reported, this value is close to 1.0, and its variation is negligible during oxygen octahedral rotation, owing to the unchanged strain state. Therefore, the octahedral tilt angle is predominantly governed by the orthorhombicity factor a_o/b_o. For a 30 uc SRO film, the measured orthorhombicity factor of 1.007 corresponds to an octahedral tilt angle of approximately 6.8°, which is slightly lower than the bulk SRO value of ~10°[22]. This comparison demonstrates that thicker films are capable of achieving octahedral distortion magnitudes close to those of bulk SRO. In contrast, the orthorhombicity factor is 1.000 for 15 uc SRO film, indicating a complete suppression of octahedral tilting in the tetragonal SRO films. Such a tetragonal phase differs fundamentally from the orthorhombic structure of bulk SRO, demonstrating that continuous oxygen octahedral connectivity across the interface modulates the phase stability of ultrathin SRO films. This underscores the vital role of the interface-tailored oxygen coordination environment in governing the structural evolution of the SRO layer. From the correlation between a_o/b_o and the SRO film thickness, the impact of the octahedral coupling can maintain about 15 uc. Given the absence of TiO_6 octahedral tilting in STO substrate, the RuO_6 tilting in the SRO film is suppressed to maintain oxygen octahedral continuity across the STO/SRO interface. This interfacial suppression effect gradually weakens with increasing distance from the interface and completely disappears beyond the critical thickness of 15 uc.

Given that the RuO_6 octahedral tilt strongly influences hybridization between Ru 4*d* and O *p* orbitals, the magnetic anisotropy of the SRO layer in STO/SRO heterostructures can be governed by the interfacial Ru-O-Ti bond angle for ultrathin SRO films. Figure 4A and B presents the *M*-*H* curves for 15 uc and 30 uc SRO

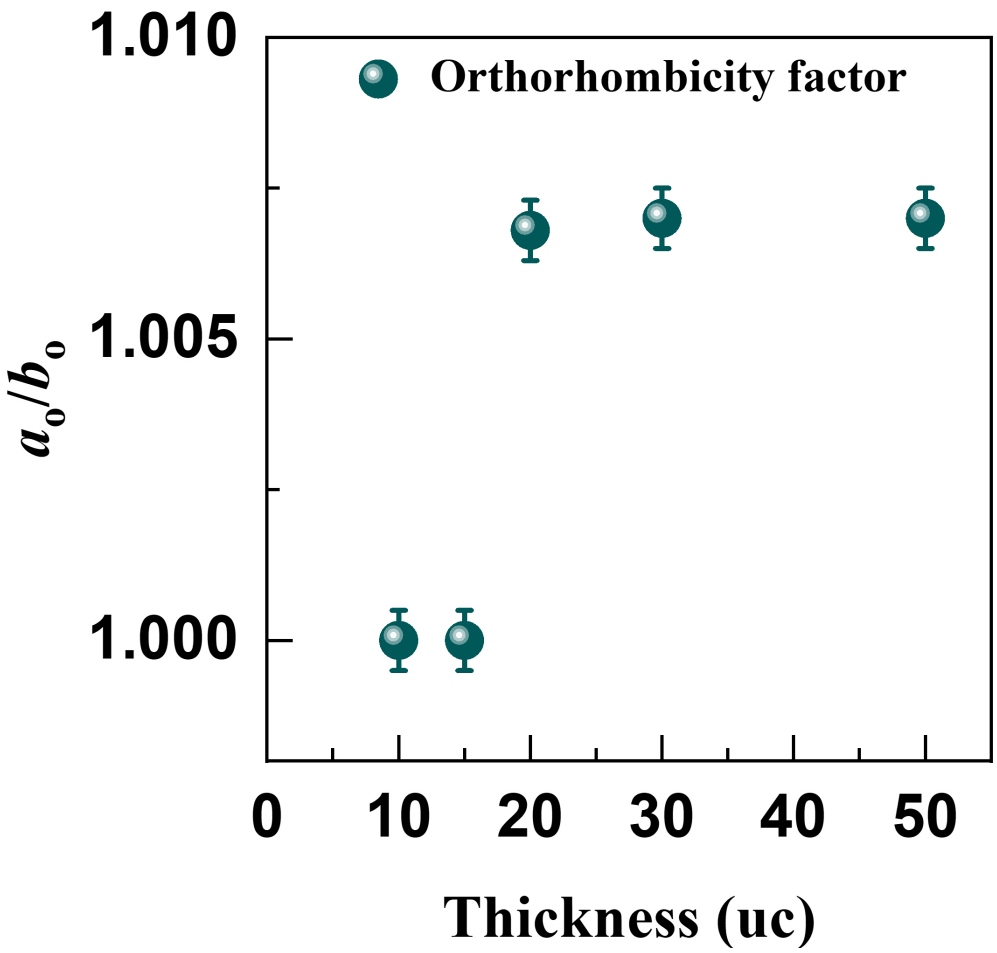

Figure 3. The orthorhombicity factor (a_o/b_o) at room temperature as a function of SRO film thickness. The abrupt change signifies a structural phase transition from tetragonal to monoclinic-distorted orthorhombic. The error bars represent the standard error, derived from the peak position of RSM measurements. SRO: $SrRuO_3$; RSM: reciprocal space mapping; uc: unit cells.

films at 10 K, respectively. The 30 uc orthorhombic SRO film exhibits an out-of-plane easy axis with a saturation magnetization of 185 emu/cm^3 and anisotropic projections along the $[1\text{-}10]_o$ {$[100]_c$} and $[001]_o$ {$[010]_c$} directions. Here c represents the pseudo-cubic structure. In contrast, the 15 uc tetragonal SRO film also exhibits an out-of-plane easy axis, accompanied by a high saturation magnetization of 330 emu/cm^3 and isotropic in-plane magnetic hysteresis loops. This distinct difference in saturation magnetization and in-plane magnetic anisotropy stems from the structural symmetry transition of SRO films. Figure 4C presents the saturation magnetization of SRO films as a function of film thickness, measured with the magnetic field applied along the STO $[001]_c$, $[100]_c$, and $[010]_c$ directions. When the field is aligned along the out-of-plane $[001]_c$ direction, the saturation magnetization decreases monotonically with increasing SRO film thickness [Supplementary Figure 4]. This trend exhibits a strong correlation with the variation of the c-axis lattice constant. Such a correlation originates from c-axis lattice elongation, which weakens the orbital overlap between Ru 4d and O 2p states along the out-of-plane direction[23]. The reduced orbital overlap suppresses the quenching of orbital magnetic moments, thereby boosting the saturation magnetization of ultrathin SRO films. In contrast, the saturation magnetization along both $[100]_c$ and $[010]_c$ directions follow a non-monotonic trend, increasing first to a maximum and then declining with increased film thickness. This transition occurs at a thickness of 15 uc, which aligns well with the structural transition from the tetragonal to the monoclinic-distorted orthorhombic phase. It is noteworthy that for film thicknesses exceeding 15 uc, the saturation magnetization along the in-plane $[100]_c$ and $[010]_c$ directions exhibit a clear separation, further

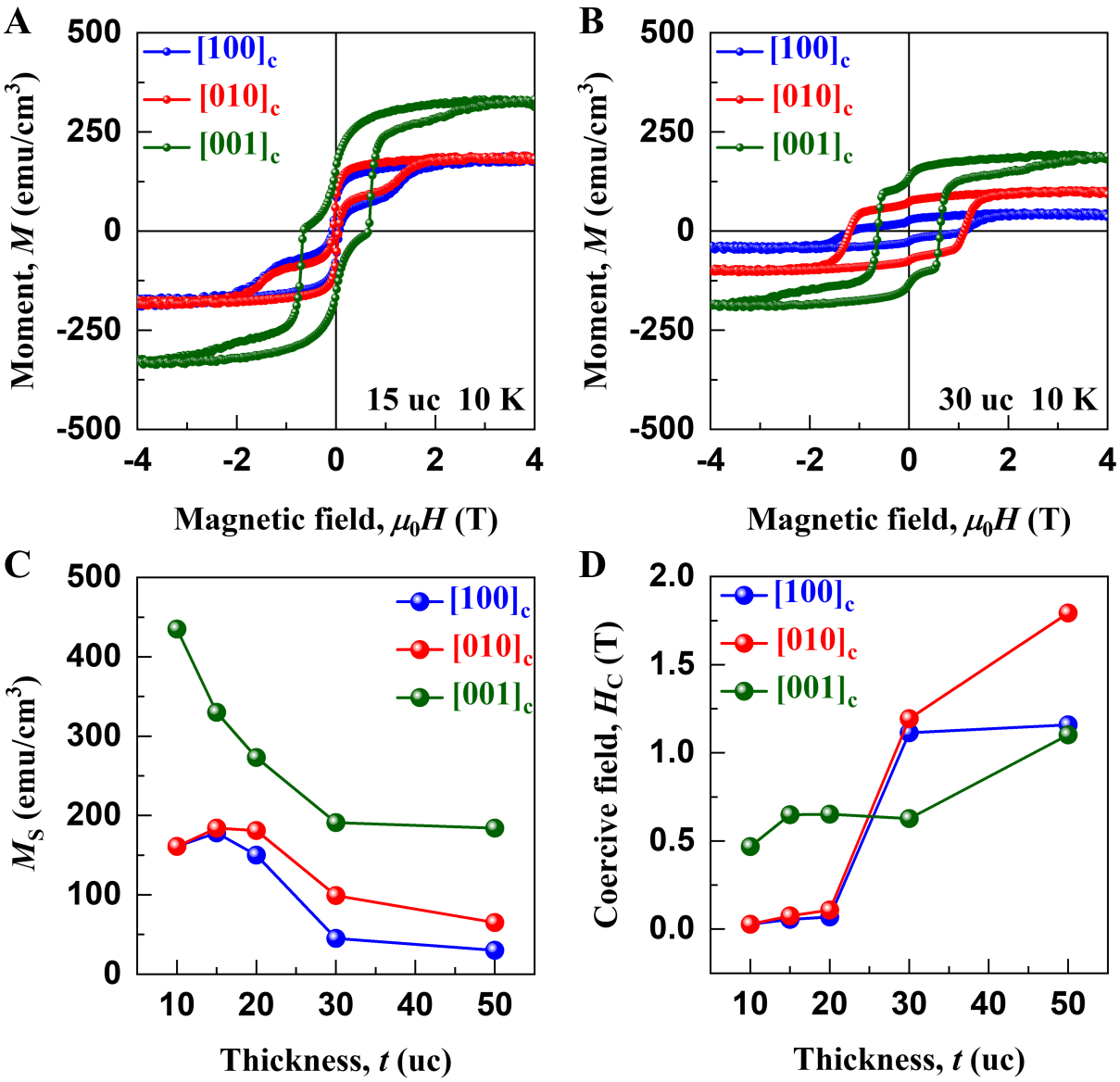

Figure 4. The curve of magnetization vs magnetic field at 10 K. (A) 15 uc and (B) 30 uc sample; (C) and (D) the saturation magnetization and coercive field as a function of the thickness of SRO film, respectively. SRO: $SrRuO_3$; uc: unit cells.

evidencing anisotropic in-plane magnetization in monoclinic-distorted orthorhombic SRO films. Such anisotropic magnetic behavior could be attributed to the symmetry change of the unit cell. Similar anisotropic behaviors, including in-plane magnetization and resistivity anisotropy, have also been reported in manganite films grown on orthorhombic substrates such as $NdGaO_3$ and $DyScO_3$[24-26]. The thickness-dependent evolution of coercivity is further presented in Figure 4D. For the out-of-plane $[001]_c$ direction, the coercivity exhibits a slight increase with increasing film thickness. In contrast, for the in-plane $[100]_c$ and $[010]_c$ directions, the coercivity presents obvious difference between the tetragonal and orthorhombic phases. The result indicates that the in-plane magnetization of tetragonal SRO films is more easily switched than that of monoclinic-distorted orthorhombic SRO films.

To elucidate the in-plane magnetic anisotropy in SRO films, we investigate its correlation with octahedral rotation, a structural modulation that couples lattice distortion to magnetic characteristics. As illustrated in Figure 2B, the Ru-O-Ru bond angle θ in tetragonal SRO films aligns along the out-of-plane direction. The

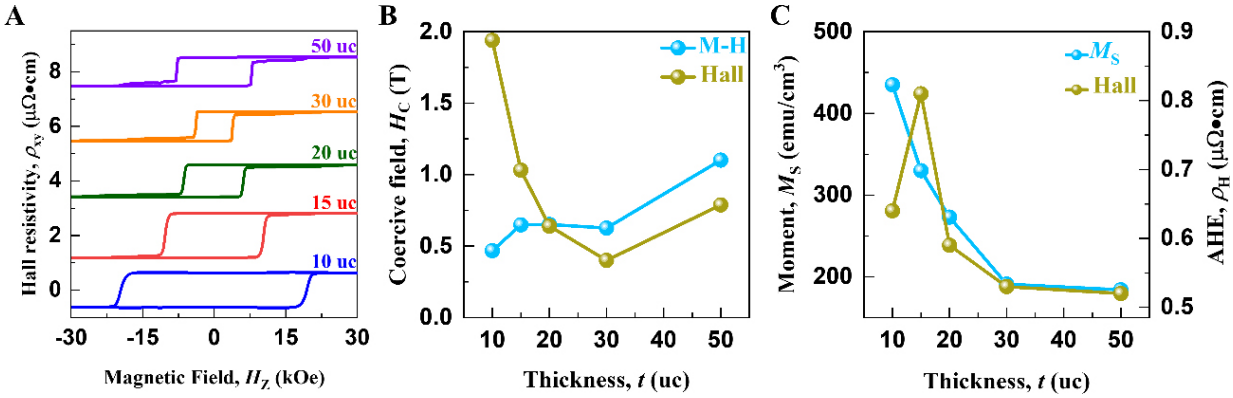

Figure 5. (A) The anomalous Hall effect (AHE) hysteresis loops for the SRO films at 10 K. Note that the OHE background and magnetoresistance contribution have already been subtracted; (B) The coercivity field of the AHE data and the out-of-plane *M-H* loops as a function of the film thickness; (C) Depiction of the saturation magnetization and saturation AHE resistivity as a function of the film thickness. SRO: $SrRuO_3$; AHE: anomalous Hall effect; OHE: ordinary Hall effect; H_Z: out-of-plane magnetic field; uc: unit cells.

crystal structure remains symmetric along the in-plane $[100]_c$ and $[010]_c$ directions, leading to isotropic in-plane magnetization. In comparison, the monoclinic-distorted orthorhombic SRO films feature an in-plane-oriented Ru-O-Ru bond angle θ that breaks the structural symmetry, thereby giving rise to anisotropic in-plane magnetic behavior [Figure 2D]. This anisotropy originates from the high susceptibility of magnetic coupling in SRO systems to the orbital overlap between Ru 4*d* and O 2*p* orbitals. In orthorhombic SRO films, the anisotropic in-plane Ru-O-Ru bonding effectively modulates such orbital overlap, which ultimately induces the formation of the anisotropic in-plane magnetic moment. The anisotropic orbital overlap also causes the low-temperature resistivity anisotropy, observed in the $La_{0.7}Sr_{0.3}MnO_3$ (LSMO) film on the $DyScO_3$ (DSO) substrate[26].

Figure 5A presents the anomalous Hall effect (AHE) measurements of SRO films at 10 K. The transverse resistivity, ρ_{xy}, of SRO films can be expressed as:

$$\rho_{xy} = \rho_{OHE} + \rho_{AHE} = R_0 H + R_A M \tag{2}$$

where $\rho_{OHE} = R_0 H$ corresponds to the ordinary Hall effect, with the ordinary Hall coefficient R_0 and the out-of-plane magnetic field H. The linear field-dependent ρ_{OHE} component has been subtracted from the raw data. Meanwhile, $\rho_{AHE} = R_A M$ represents the AHE, where R_A is the anomalous Hall coefficient and M is the out-of-plane magnetization. The anomalous component of transverse Hall resistivity ρ_{xy} as a function of H_Z exhibits nearly 100% remanence and sharp magnetization reversal for all measured samples, indicative of robust perpendicular magnetic anisotropy (PMA). Notably, the tetragonal SRO film exhibits a distinct discrepancy in coercivity between the AHE measurement and the out-of-plane *M-H* curve [Figure 5B]. As displayed in Supplementary Figure 5, the out-of-plane *M-H* loop of the 10 uc SRO film can be decomposed into two superimposed hysteresis components: M_I-H with low coercivity and high saturation magnetization, and M_T-H with high coercivity and low saturation magnetization. The out-of-plane *M-H* loop was fitted using[27]:

$$M(H) = M_{S-I} \times \tanh\left(\frac{H \pm H_{c-I}}{H_I}\right) + M_{S-T} \times \tanh\left(\frac{H \pm H_{c-T}}{H_T}\right) \tag{3}$$

where the first and second terms on the two *M-H* contributions: M_I-H and M_T-H loops. M_{S-I} (M_{S-T}) and H_{c-I} (H_{c-T}) are the saturation magnetization and coercivity, respectively, of the M_I-H (M_T-H) loop. H_I and H_T are two fitting constants. The coercivity values extracted from AHE measurements are highly consistent with

those of the M_T-H component. As reported in previous studies, M_I-H response originates from the interfacial ferromagnetic insulating phase of the SRO layer. This phase emerges within the 3-4 uc region near the substrate interface due to abundant oxygen vacancies[28,29]. Such an interfacial phase makes no contribution to the AHE signal. Although the M_I-H component exists in SRO films of all thicknesses, its relative contribution gradually declines as the film thickness increases. According to Equation 2, the saturation anomalous Hall resistivity, ρ_H, should be proportional to the saturation magnetization. Nevertheless, an obvious discrepancy between the trends of ρ_H and the saturation magnetization is observed in the tetragonal SRO film [Figure 5C]. This abnormal phenomenon can be attributed to a significant contribution from the interfacial insulating phase to the magnetic moment in ultrathin films.

CONCLUSIONS

In summary, we realize atomic-scale modulation of magnetic anisotropy in SRO thin films via thickness-engineered structural phase transition. The cubic STO substrate effectively suppresses RuO_6 octahedral tilting at the heterointerface, which stabilizes the tetragonal phase in ultrathin SRO films below the critical thickness. Such tetragonal symmetry endows the films with enhanced saturation magnetization and isotropic in-plane magnetic behavior. In contrast, SRO films thicker than the critical dimension undergo a structural transition to the monoclinic-distorted orthorhombic phase, triggering the emergence of prominent in-plane magnetic anisotropy. These findings demonstrate that precise modulation of oxygen octahedral coupling at oxide heterointerfaces offers an effective strategy for artificially tailoring the functional magnetic properties of correlated oxide systems.

DECLARATIONS

Acknowledgments

The authors thank the support of SUSTech Core Research Facilities.

Authors' contributions

Made substantial contributions to the conception and design of the study and performed data analysis and interpretation, writing-original draft: Xu, Z.

Performed data acquisition and provided administrative, technical, and material support: Chai, L.; Hu, S.; Ye, M.; Chen, S.

Funding, source, and supervisor: Jiang, Y.; Chen, L.

Availability of data and materials

The data supporting the findings of this study are available within this Article and its Supplementary Materials. Further data are available from the corresponding authors upon request.

AI and AI-assisted tools statement

Not applicable.

Financial support and sponsorship

This work is supported partially by National Key Research and Development Program of China (Nos. 2022YFA1204003, 2022YFA1402903, 2022YFA1402601), National Natural Science Foundation of China (Nos. 52271186, 52571230, U24A6002, 12574096, 12504076), Tianjin Key Laboratory of Optoelectronic Detection Technology and System (No. 2024LODTS101), Shenzhen Fundamental Research Program (Grant No. JCYJ20250604144519025).

Conflicts of interest

All authors declared that there are no conflicts of interest.

Ethical approval and consent to participate

Not applicable.

Consent for publication

Not applicable.

Copyright

© The Author(s) 2026.

Supplementary Materials

Supplementary Materials

REFERENCES

1. Keimer, B.; Moore, J. E. The physics of quantum materials. *Nat. Phys.* **2017**, *13*, 1045-55. DOI
2. Tokura, Y.; Kawasaki, M.; Nagaosa, N. Emergent functions of quantum materials. *Nat. Phys.* **2017**, *13*, 1056-68. DOI
3. Linder, J.; Robinson, J. W. A. Superconducting spintronics. *Nat. Phys.* **2015**, *11*, 307-15. DOI
4. Šmejkal, L.; Sinova, J.; Jungwirth, T. Beyond conventional ferromagnetism and antiferromagnetism: a phase with nonrelativistic spin and crystal rotation symmetry. *Phys. Rev. X.* **2022**, *12*, 031042. DOI
5. Song, C.; Bai, H.; Zhou, Z.; et al. Altermagnets as a new class of functional materials. *Nat. Rev. Mater.* **2025**, *10*, 473-85. DOI
6. Maeno, Y.; Ikeda, A.; Mattoni, G. Thirty years of puzzling superconductivity in Sr_2RuO_4. *Nat. Phys.* **2024**, *20*, 1712-8. DOI
7. Grinenko, V.; Das, D.; Gupta, R.; et al. Unsplit superconducting and time reversal symmetry breaking transitions in Sr_2RuO_4 under hydrostatic pressure and disorder. *Nat. Commun.* **2021**, *12*, 3920. DOI PubMed PMC
8. Grinenko, V.; Ghosh, S.; Sarkar, R.; et al. Split superconducting and time-reversal symmetry-breaking transitions in Sr_2RuO_4 under stress. *Nat. Phys.* **2021**, *17*, 748-54. DOI
9. Itoh, S.; Endoh, Y.; Yokoo, T.; et al. Weyl fermions and spin dynamics of metallic ferromagnet $SrRuO_3$. *Nat. Commun.* **2016**, *7*, 11788. DOI PubMed PMC
10. Lin, W.; Liu, L.; Liu, Q.; et al. Electric field control of the magnetic Weyl fermion in an epitaxial $SrRuO_3$ (111) thin film. *Adv. Mater.* **2021**, *33*, e2101316. DOI
11. Kar, U.; Singh, A. K.; Hsu, Y.; et al. The thickness dependence of quantum oscillations in ferromagnetic Weyl metal $SrRuO_3$. *npj. Quantum. Mater.* **2023**, *8*, 540. DOI
12. Lu, W.; Yang, P.; Song, W. D.; Chow, G. M.; Chen, J. S. Control of oxygen octahedral rotations and physical properties in $SrRuO_3$ films. *Phys. Rev. B.* **2013**, 88. DOI
13. Lu, W.; Dong Song, W.; He, K.; et al. The role of octahedral tilting in the structural phase transition and magnetic anisotropy in $SrRuO_3$ thin film. *J. Appl. Phys.* **2013**, *113*, 063901. DOI
14. Koster, G.; Klein, L.; Siemons, W.; et al. Structure, physical properties, and applications of $SrRuO_3$ thin films. *Rev. Mod. Phys.* **2012**, *84*, 253-98. DOI
15. Singh, A. K.; Yang, S.; Kar, U.; et al. Evolution of the structural phase and orientation in ultrathin $SrRuO_3$ film with $SrTiO_3$ capping layer. *Sci. Rep.* **2025**, *15*, 17841. DOI PubMed PMC
16. Rondinelli, J. M.; Spaldin, N. A. Structure and properties of functional oxide thin films: insights from electronic-structure calculations. *Adv. Mater.* **2011**, *23*, 3363-81. DOI PubMed
17. Kan, D.; Aso, R.; Sato, R.; Haruta, M.; Kurata, H.; Shimakawa, Y. Tuning magnetic anisotropy by interfacially engineering the oxygen coordination environment in a transition metal oxide. *Nat. Mater.* **2016**, *15*, 432-7. DOI
18. Jeong, S. G.; Han, G.; Song, S.; et al. Propagation control of octahedral tilt in $SrRuO_3$ via artificial heterostructuring. *Adv. Sci.* **2020**, *7*, 2001643. DOI
19. Lee, S. A.; Oh, S.; Hwang, J.; et al. Enhanced electrocatalytic activity via phase transitions in strongly correlated $SrRuO_3$ thin films. *Energy. Environ. Sci.* **2017**, *10*, 924-30. DOI
20. Kan, D.; Aso, R.; Kurata, H.; Shimakawa, Y. Epitaxial strain effect in tetragonal $SrRuO_3$ thin films. *J. Appl. Phys.* **2013**, *113*, 173912. DOI
21. Chang, S. H.; Chang, Y. J.; Jang, S. Y.; et al. Thickness-dependent structural phase transition of strained $SrRuO_3$ ultrathin films: the role of octahedral tilt. *Phys. Rev. B.* **2011**, *84*, 104101. DOI
22. Zayak, A. T.; Huang, X.; Neaton, J. B.; Rabe, K. M. Structural, electronic, and magnetic properties of $SrRuO_3$ under epitaxial strain. *Phys. Rev. B.* **2006**, *74*, 094104. DOI

23. Grutter, A. J.; Wong, F. J.; Jenkins, C. A.; Arenholz, E.; Vailionis, A.; Suzuki, Y. Stabilization of spin-zero Ru^{4+} through epitaxial strain in $SrRuO_3$ thin films. *Phys. Rev. B.* **2013**, *88*, 214410. DOI
24. Liao, Z.; Huijben, M.; Zhong, Z.; et al. Controlled lateral anisotropy in correlated manganite heterostructures by interface-engineered oxygen octahedral coupling. *Nat. Mater.* **2016**, *15*, 425-31. DOI
25. Zhou, G.; Ji, H.; Yan, Z.; et al. Interfacial engineering manipulation of magnetic anisotropy evolution via orbital reconstruction in low-dimensional manganite superlattices. *Sci. China. Mater.* **2022**, *65*, 1902-11. DOI
26. Wang, B.; You, L.; Ren, P.; et al. Oxygen-driven anisotropic transport in ultra-thin manganite films. *Nat. Commun.* **2013**, *4*, 2778. DOI PubMed PMC
27. Li, P.; Ding, J.; Zhang, S. S.; et al. Topological hall effect in a topological insulator interfaced with a magnetic insulator. *Nano. Lett.* **2021**, *21*, 84-90. DOI
28. Ishigami, K.; Yoshimatsu, K.; Toyota, D.; et al. Thickness-dependent magnetic properties and strain-induced orbital magnetic moment in $SrRuO_3$ thin films. *Phys. Rev. B.* **2015**, *92*, 064402. DOI
29. Shen, X.; Qiu, X.; Su, D.; Zhou, S.; Li, A.; Wu, D. Thickness-dependent metal-insulator transition in epitaxial $SrRuO_3$ ultrathin films. *J. Appl. Phys.* **2015**, *117*, 015307. DOI

Disclaimer/Publisher's Note: All statements, opinions, and data contained in this publication are solely those of the individual author(s) and contributor(s) and do not necessarily reflect those of OAE and/or the editor(s). OAE and/or the editor(s) disclaim any responsibility for harm to persons or property resulting from the use of any ideas, methods, instructions, or products mentioned in the content.

© The Author(s) 2026. Open Access This article is licensed under a Creative Commons Attribution 4.0 International License (https://creativecommons.org/licenses/by/4.0/), which permits unrestricted use, sharing, adaptation, distribution and reproduction in any medium or format, for any purpose, even commercially, as long as you give appropriate credit to the original author(s) and the source, provide a link to the Creative Commons license, and indicate if changes were made.